JOURNAL OF SOLID STATE CHEMISTRY 7, 94–105 (1973)

High Resolution Electron Microscopy of $TiO_2 \cdot 7Nb_2O_5$

S. IIJIMA*

Department of Physics, Arizona State University, Tempe, Arizona 85281

AND

J. G. ALLPRESS

Division of Tribophysics, CSIRO, University of Melbourne, Parkville, Vic. 3052, Australia

Received August 21, 1972

The defect structure of $TiO_2 \cdot 7Nb_2O_5$ has been examined at about 0.3 nm resolution in an electron microscope. Under suitable conditions of crystal orientation and objective lens defocus, the contrast in images from very thin fragments can be interpreted directly in terms of structure. Proposed structures for Wadsley intergrowth defects and displacements are confirmed, and new observations of complex fault bands and grain boundaries are described. Microdomains of $TiNb_{14}O_{37}$, with the structure predicted by Wadsley, have also been found in this material.

1. Introduction

The oxides and oxyfluorides of niobium have long been known as nonstoichiometric compounds. Until recently, they were considered to retain the same structure virtually unchanged over a wide range of chemical composition, with accompanying variations in the concentration of vacancies or interstitial atoms. However, careful X-ray studies by Wadsley and coworkers (*1*) established that there are a large number of distinct but closely related phases, each of specific composition, lying within what was previously regarded as a homogeneous series of solid solutions. Subsequently, a series of electron optical studies (*2–4*) has shown that even smaller changes of composition are accommodated by the coherent intergrowth, at the unit cell level, of planar slabs of one structure in a matrix of another.

The electron optical studies have indicated that under appropriate experimental conditions, the contrast in lattice images of these materials can be directly correlated to structural features. Computations of the contrast expected in a relatively simple case (*5*) have confirmed that these correlations are justified. However, until very recently, the resolution of the experimental work was sufficient to reveal only the gross features of the structures, in particular, the crystallographic shear (CS) planes. With careful use of high resolution (about 0.3 nm) microscopy, it has now been possible to reveal the arrangement of metal atoms directly, in the unit cell of $Ti_2Nb_{10}O_{29}$ (*6*, *7*). This technique should be of considerable value, both for the study of the nature of defects in these materials, and in favorable cases, for the direct determination of crystalline structure.

The present paper describes in detail, some high resolution observations of a quenched specimen of the composition $TiO_2 \cdot 7Nb_2O_5$. The sample had been prepared by the late Dr. A. D. Wadsley, in an attempt to obtain the compound $TiNb_{14}O_{37}$ (*8*), a possible member of the homologous series $M_{3n}O_{8n-3}$ (M = metal) with $n = 5$, extending from the known phases $TiNb_2O_7$ ($n = 3$) and $Ti_2Nb_{10}O_{29}$ ($n = 4$). It was subsequently examined in an electron microscope at relatively poor resolution (*4*, *9*) and some of the simpler defect structures were identified and described. The present study confirms most of

* On leave from Research Institute for Scientific Measurements, Tohoku University, Sendai, Japan.

the earlier work, and extends the number of observations of complex defects. The higher resolution has enabled us to describe the structure of complex arrays of faults with confidence, and to detect domains of $TiNb_{14}O_{37}$, having the structure predicted by Wadsley.

2. Experimental Methods

The sample of $TiO_2 \cdot 7Nb_2O_5$ was originally prepared from the constituent oxides by sintering a ground mixture at 1700 K for 16 hr in air, and quenching the product. A portion of the sample was ground in an agate mortar, and dispersed in methyl chloroform or acetone. One drop of the suspension was collected on a carbon supporting film which contained a number of holes of 0.1–10 μm diameter. Crystals which had very thin edges projecting over these holes were sought; and only those which could be tilted and rotated until the electron beam was incident parallel to their short *b* axes, were examined further. Under these conditions, the diffraction patterns contained only *h0l* reflections.

Observations were made with a JEM-100B (100 kV) electron microscope, equipped with a goniometer stage ($\pm 30°$ tilt). A special anti-contamination device, and pointed filaments, were used. The objective aperture was 40 μm in diameter, and it included beams diffracted from planes with spacings greater than about 0.3 nm. Most of the micrographs were recorded at a magnification of 420,000×.

It was found previously (*7*) that the appearance of the images was very dependent on the orientation of the crystal, and on the extent of defocusing of the objective lens. The discussion below is restricted to images from crystals aligned with their *b* axes parallel to the direction of the incident electron beam, to within 10^{-3} rad. The optimum extent of defocus was found to lie in the range from about 50 to 90 nm underfocus.

Experimentally, the contrast was observed to vary dramatically with crystal thickness, and the unit cell structure could only be distinguished reliably in edge regions of the crystal fragments. The thickness of these regions is difficult to estimate, but is probably of the order of 10 nm or less.

In order to obtain results which are representative of the whole sample, it is desirable to examine a large number of fragments. The experimental problems make this goal difficult to achieve. Less than 0.1% of the crystals on a specimen grid were suitably thin and appropriately oriented for detailed examination, and the observations were therefore restricted to about 60 fragments.

Previous observations (*10*) have indicated that these materials are not plastically deformed by grinding, and that no additional defects are introduced during preparation of the specimens for electron microscopy. The high resolution observations confirmed this, although there were some indications that metal atoms located in very thin edge regions of crystals were sometimes rearranged slightly. Furthermore, there was no evidence of radiation damage during observation.

3. Results and Interpretation

The composition $TiO_2 \cdot 7Nb_2O_5$ (i.e., 87.5 mole% Nb_2O_5) lies between those of the well-characterized phases $TiNb_{24}O_{62}$ (*11*) (92.4 mole% Nb_2O_5) and $Ti_2Nb_{10}O_{29}$ (*8*) (71.5 mole% Nb_2O_5) The sample was far from homogeneous, and it is convenient to describe most of the results in terms of the matrix phase which predominated in any particular fragment. This phase was most commonly $TiNb_{24}O_{62}$, but 5 of the 60 fragments were more closely related to $Ti_2Nb_{10}O_{29}$. Models for the simpler defects in both these matrices have been described previously (*4*, *9*) and a brief account of the high resolution results which confirm these models will be given first. New observations of domains of $TiNb_{14}O_{37}$, fault bands, and a grain boundary will then be considered in more detail.

3.1. The $TiNb_{24}O_{62}$ Matrix

An idealized representation of the structure of $TiNb_{24}O_{62}$ (*11*) is shown in Fig. 1a. It contains 3×4 blocks of corner-shared metal–oxygen octahedra, extending parallel to *b*. The blocks drawn dark and light are centered $b/2$ (≈ 0.19 nm) apart, and are joined to one another by edge-sharing of octahedra, along the crystallographic shear (CS) planes (arrowed). The CS planes parallel to *a* are of two types, labeled *E* and *F*. Adjacent blocks along *F* planes are joined by edge-sharing of octahedra, but in *E* planes, they are separated by metal atoms in tetrahedral coordination (circles). A simpler representation of the same structure, in which each block of octahedra is drawn as a rectangle, is shown in Fig. 1b. The unit cell dimensions of $TiNb_{24}O_{62}$ (*11*) are $a = 2.978$ nm, $b = 0.382$ nm, $c = 2.112$ nm, $\beta = 94.9°$; space group *C2*.

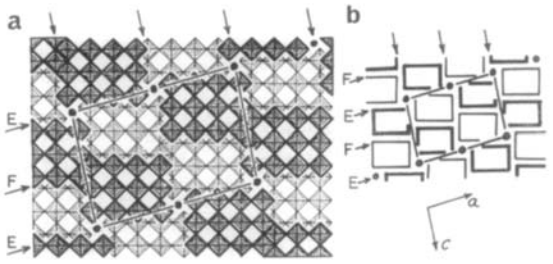

FIG. 1. Idealized representations of the structure of $TiNb_{24}O_{62}$. (a) Each hatched square represents an octahedron of six oxygen atoms surrounding a central metal atom, viewed down a body diagonal. The octahedra are joined by sharing corners into blocks of 4×3, extending along b. The metal atoms in darker and lighter blocks lie at $y = 0$ and $\frac{1}{2}$, respectively, and adjacent blocks are joined along crystallographic shear (CS) planes (arrowed) by edge-sharing of octahedra. (●) Metal atoms in tetrahedral coordination, which lie in alternate CS planes parallel to a, marked E. (b) Each block of 4×3 octahedra is represented by a rectangle, and the tetrahedral sites (●).

An underfocus two-dimensional lattice image in which this structure is clearly revealed is reproduced in Fig. 2. The image contrast consists of rectangular elements, each of which contains a set of six white dots in two rows of three, corresponding to the six empty channels parallel to b which occur in each 4×3 block of octahedra in the structure (Fig. 1a). Dark lines occur where the rectangular elements are joined; i.e., where the octahedra share edges, and the metal atoms are only about 0.2 nm apart in projection, compared with 0.38 nm within the blocks. The tetrahedral sites appear as very dark blobs along the lines marked E.

The detail with which the various structural elements are resolved is quite critically dependent on focusing conditions and crystal orientation, and hence differs slightly in different micrographs. For example, the empty channels in groups of six are more apparent in Fig. 3b than in Fig. 2, but are barely visible in Fig. 5c. On the other hand, the positions of the tetrahedral sites stand out more clearly in the latter micrograph. In previous studies at poorer resolution, only the tetrahedral sites, which are widely separated, were easily identified in images at this orientation (*9*, *12*).

Concurrent with the experimental studies, computations of the contrast expected in lattice images of this material are being made (*13*), and an example which shows fair agreement with experiment is inset in Fig. 2. This image was

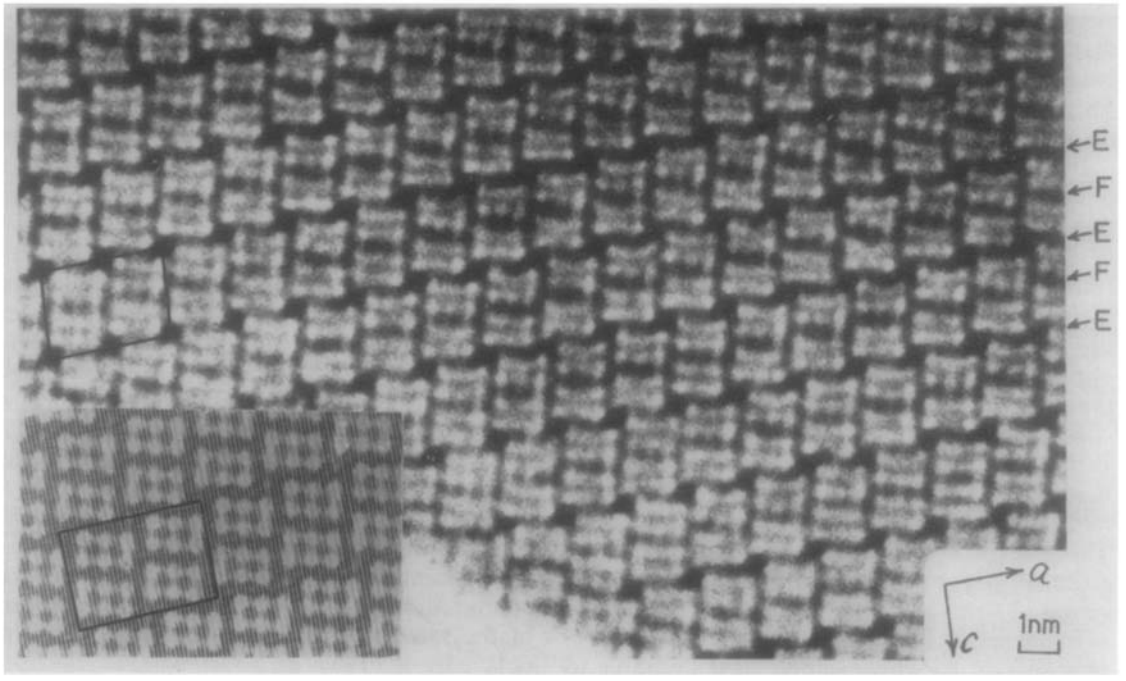

FIG. 2. Two-dimensional lattice image from a fragment of $TiNb_{24}O_{62}$, recorded at the same orientation as that of the model in Fig. 1. Some of the E and F type CS planes are identified. The inset shows the contrast computed for a crystal of $TiNb_{24}O_{62}$, 8 nm thick, imaged 50 nm underfocus, using 65 contributing $h0l$ beams.

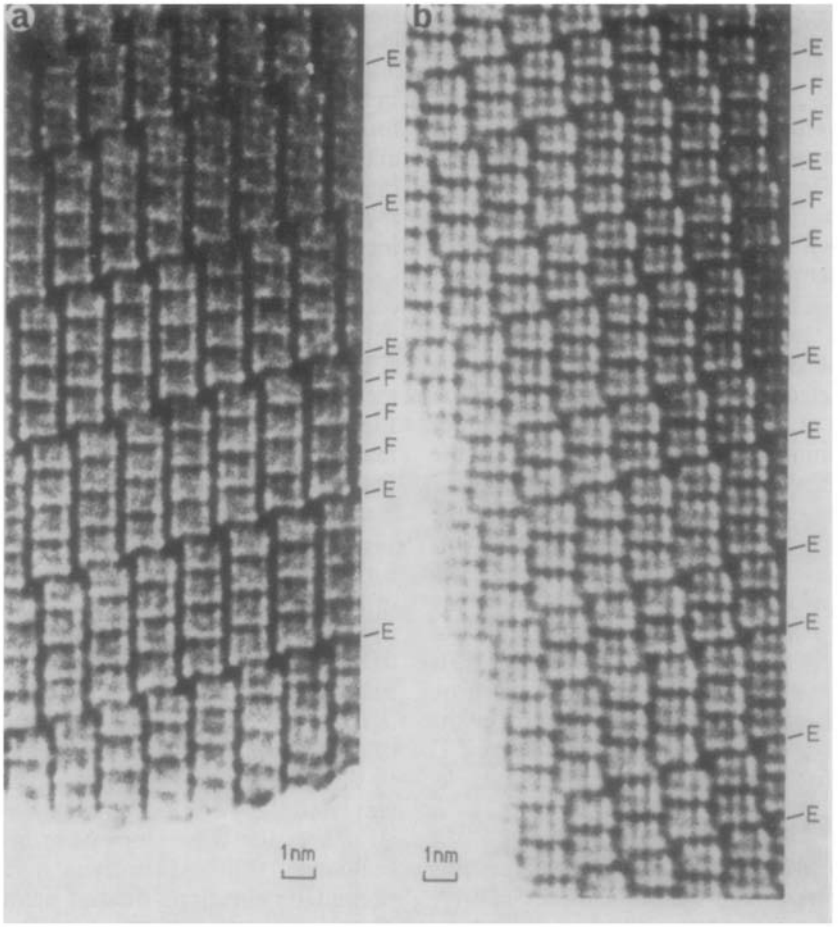

FIG. 3. Lattice images from fragments of nominal composition $TiO_2 \cdot 7Nb_2O_5$, showing several ordered intergrowths of the parent structures, $M_{13}O_{33}$ and $M_{12}O_{29}$, identified by their corresponding CS planes, labeled *E* and *F*, respectively. (a) Four periods of the sequence *–E–3F–E–*, having the composition $Ti_5Nb_{44}O_{120}$. (b) Four periods of the sequence *–E–F–E–2F–E–*, with the composition $Ti_4Nb_{58}O_{153}$.

computed using the published atomic positions in $TiNb_{24}O_{62}$ (*11*), for a crystal 8 nm thick, imaged 50 nm underfocus from the Gaussian image plane, and with 65 contributing *h*0*l* beams. The results confirm our experimental observation that under appropriate conditions, there is a 1 : 1 correspondence between image contrast and structure. The calculations are a straightforward extension to two dimensions from the simpler case of a crystal oriented so that diffracted beams from a systematic set (e.g., *h*00 or 00*l*) contribute to the image (*14*, *15*).

3.1.1. *Wadsley Defects*

a. Intergrowth of $Ti_2Nb_{10}O_{29}$. The structure of $TiNb_{24}O_{62}$ may itself be regarded as an intergrowth of two simpler structures; $M_{13}O_{33}$ (M = metal), containing only *E* type CS planes, and $M_{12}O_{29}$, containing only *F* type CS planes (*4*). We have already shown (*4*) how the *–E–F–E–F–* sequence of planes in $TiNb_{24}O_{62}$ can be modified by the insertion of additional *F* planes in a coherent manner, and that most of the discrepancy in composition between $TiO_2 \cdot 7Nb_2O_5$ and $TiNb_{24}O_{62}$ is accommodated in this way. The additional *F* planes frequently occur in more complex ordered sequences. The high resolution images in Fig. 3 confirm the previous structural models, and illustrate some of these sequences. In each case, the *E* and *F* planes are easily identified, and four periods of the sequences *–E–3F–E–* and *–E–F–E–2F–E–* can be distinguished in (a) and (b), respectively. These intergrowths correspond to compositions

of $Ti_5Nb_{44}O_{120}$ and $Ti_4Nb_{58}O_{153}$, respectively, and their periodicities are about 4.4 and 5.6 nm, respectively. Structures which can be described as *–E–2F–E–*, *–E–4F–E–*, *–E–5F–E–*, and *–E–6F–E–* were also observed, but the extent and perfection of domains was greatly reduced as the periodicity increased.

b. Intergrowth of H–Nb_2O_5. The composition region between Nb_2O_5 and $TiNb_{24}O_{62}$ is known to exhibit intergrowth of the latter structure and that of the high temperature (H-) form of Nb_2O_5. We did not anticipate observing such intergrowth in the present sample; nevertheless, we found one defect, marked H in Fig. 4a, which had this type of structure. The defect is a slab of material running parallel to the *c* axis of the matrix, containing alternately 4×3 and 5×3 blocks. Its presence causes a displacement of the *E* and *F* planes, which lie approximately perpendicular to it. A model for this type of intergrowth is shown in Fig. 4b—the structure of the defect slab is exactly the same as that of a slab of H–Nb_2O_5, one unit cell along *c* wide (*16*). Its presence in a specimen of nominal composition $TiO_2 \cdot 7Nb_2O_5$ serves to indicate that under the conditions of preparation, the distribution of Ti and Nb atoms varied widely within the sample.

3.1.2. Displacements

Next to Wadsley defects, the most commonly observed faults in the quenched material were displacements of CS planes. Models which have been proposed for these defects (*9*) involve the inclusion of a single column of blocks of either 3×3 or 5×3 octahedra, extending parallel to *b* in the matrix of 4×3 blocks. These defects were found on *E* planes containing tetrahedral sites, and their presence displaced the planes across the defect columns. Direct confirmation of these models was obtained from high resolution images, such as those reproduced in Fig. 5.

Figure 5a shows five 3×3 blocks (circled), and each of these has two tetrahedral sites associated with it, diagonally across the block. Some of the *E* and *F* planes are identified, and their displacements at the 3×3 blocks are clear. The model in Fig. 5b shows how these blocks are built into the matrix. The displacements associated with the insertion of single and double columns of 5×3 blocks can be seen in the encircled areas of Fig. 5c, and a model of the double column case (upper right) is shown in Fig. 5d. The intergrowth of a slab of H–Nb_2O_5 (Fig. 4a) may be regarded as an extreme example of this, where the insertion of 5×3 blocks is ordered and every *E* plane suffers the same displacement.

In a number of cases, the contrast in the vicinity of a displacement indicated the presence of a step in the columns of 3×3 or 5×3 blocks, as they traversed the fragments in the *b* direction. Likely structures for these steps have been postulated previously (*9*), and because in this case, the present observations do not provide any additional information, they are not discussed further.

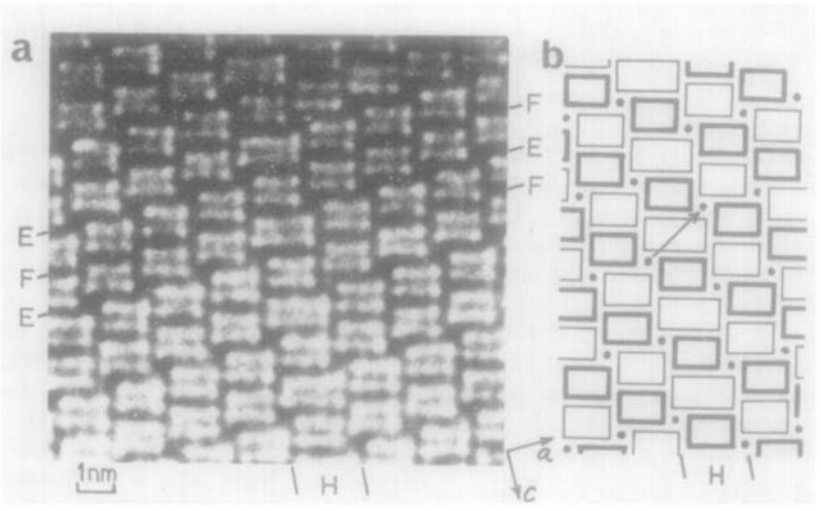

FIG. 4a. Lattice image, showing intergrowth of a slab of H-Nb_2O_5, marked H, in a matrix of $TiNb_{24}O_{62}$. (b) Idealized model of the slab H and the surrounding matrix. The arrow indicates the displacement of an *E* plane across a 5×3 block in H. The axes refer to the matrix.

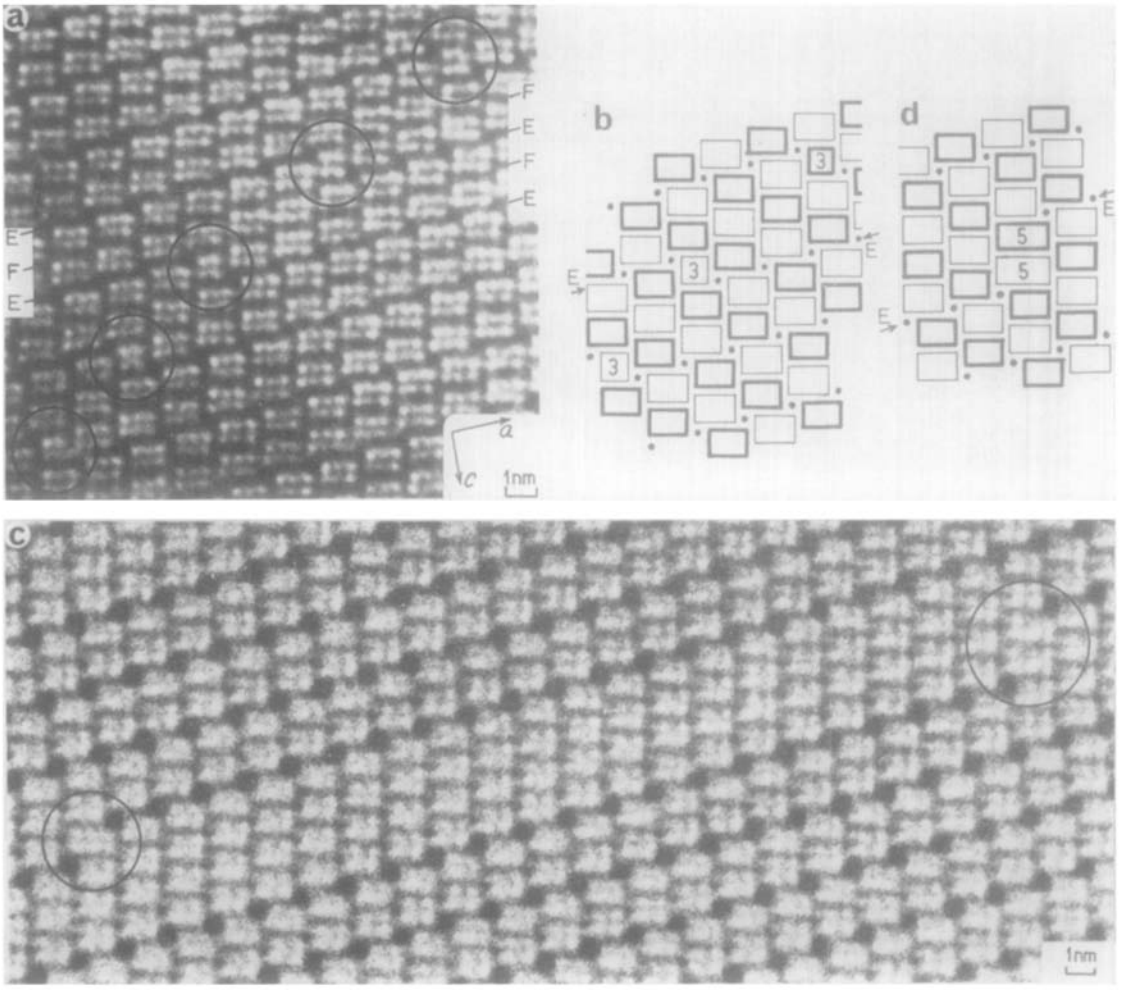

FIG. 5a. Lattice image, showing the incorporation of five 3×3 blocks (circled) in a matrix of $TiNb_{24}O_{62}$. Their presence displaces the *E* and *F* planes, some of which are identified. (b) Idealized model, showing how the three 3×3 blocks in the central part of (a) are built into the matrix. (c) Lattice image, showing displacements along *E* planes containing tetrahedral sites (dark blobs), associated with the presence of 5×3 blocks (circled). (d) Model of the displacement caused by the double 5×3 block at the top right of (c).

3.2. The Monoclinic $Ti_2Nb_{10}O_{29}$ Matrix

Of the five fragments of $Ti_2Nb_{10}O_{29}$ which were found in the sample, four had the monoclinic structure (*8*), and only one was orthorhombic. Diffraction patterns from the monoclinic crystals always contained streaks parallel to c^*, and the images confirmed previous conclusions (*4*) that they were due to the presence of microdomains of the orthorhombic polymorph, often only 1 unit cell in width. These defects do not alter the composition of the crystal, and they may be regarded as stacking faults on (001) planes, in which the stacking units are the slabs of 4×3 blocks which extend parallel to *a* through the structure.

Wadsley defects consisting of slabs of 4×4 blocks were often found intergrown in domains of monoclinic $Ti_2Nb_{10}O_{29}$, and an example is shown in Fig. 6. These defects were identified earlier (*9*) as slabs of the N form of Nb_2O_5 (*17*), and the model which was proposed for them is consistent with the present observations.

3.3. The Existence of $TiNb_{14}O_{37}$

Wadsley's aim in preparing the sample which we have been examining was to obtain $TiNb_{14}O_{37}$,

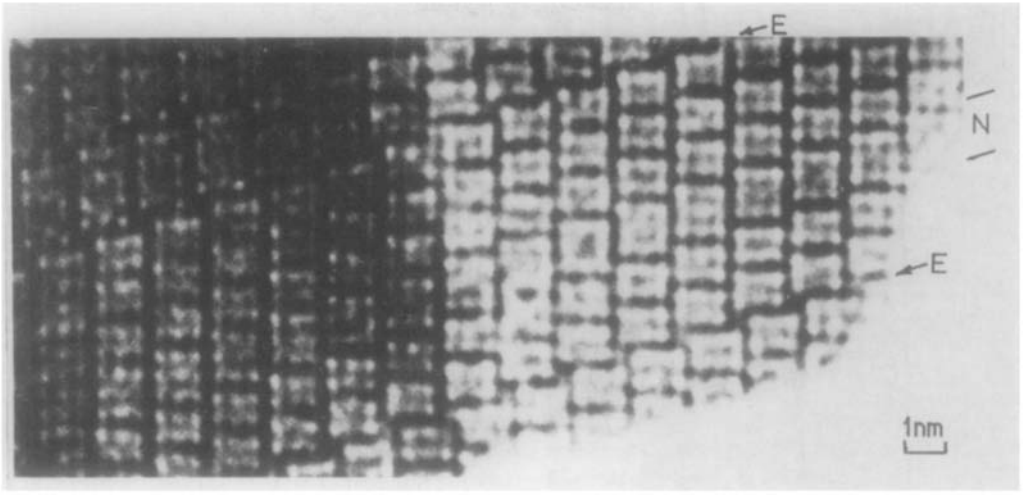

FIG. 6. Lattice image, showing the intergrowth of a slab of 4 × 4 blocks of the N-Nb_2O_5 structure, labeled N, in a microdomain of $Ti_2Nb_{10}O_{29}$. The planes marked *E* define the boundaries of this microdomain.

and he postulated (*8*) that it should possess the structure shown schematically in Fig. 7b (center). It is built from 5 × 3 blocks, but is otherwise similar in all respects to monoclinic $Ti_2Nb_{10}O_{29}$ (4 × 3 blocks, Fig. 7b, left) and $TiNb_2O_7$ [3 × 3 blocks (*18*)]. The compound $MgNb_{14}O_{35}F_2$ was recently found to have this structure (*19*).

Figure 7a shows a domain of 5 × 3 blocks

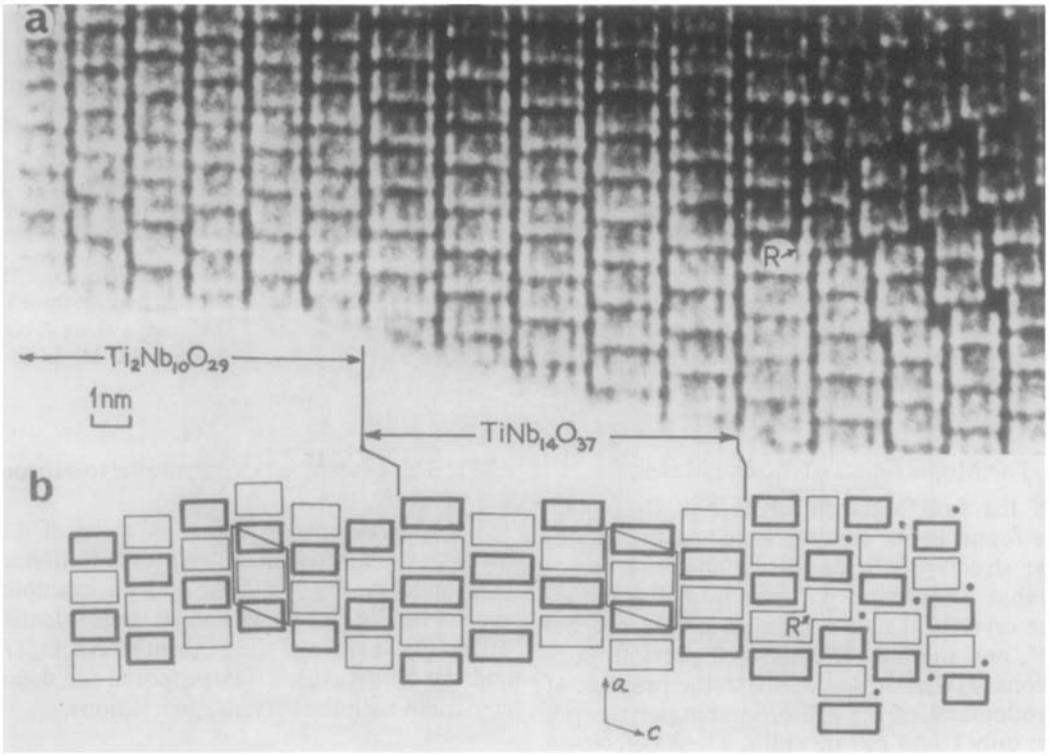

FIG. 7a. Lattice image, showing a microdomain of $TiNb_{14}O_{37}$, built from 5 × 3 blocks, intergrown with $Ti_2Nb_{10}O_{29}$ (4 × 3 blocks) on the left, and faulted $TiNb_{24}O_{62}$ on the right. (b) Model of the same area. The unit cells of $TiNb_{14}O_{37}$ (center) and $Ti_2Nb_{10}O_{29}$ (left) are outlined.

(center), arranged as Wadsley suggested for $TiNb_{14}O_{37}$, surrounded by regions of monoclinic $Ti_2Nb_{10}O_{29}$ (left) and faulted $TiNb_{24}O_{62}$ (right). The estimated unit cell dimensions are $a = 2.05$ nm, $b = 0.38$ nm, $c = 1.93$ nm, $\beta = 109°$, in good agreement with Wadsley's predicted data (*8*), after transforming the latter to the standard space group $C2/m$. The model in Fig. 7b indicates how this structure is coherently intergrown with those on either side of it in the region included in Fig. 7a. Some aspects of this model are referred to below.

More restricted regions of the same structure, such as are shown in Fig. 8a, were often observed. The presence of single or multiple slabs of 5×3 blocks has the effect of displacing E type CS planes over large distances, but they are basically similar to the single and double column displacements shown in Fig. 5c. In each case, the E plane is interrupted at one corner of the region of 5×3 blocks, and continues again from the diagonally opposite corner, as the model in Fig. 8b indicates.

3.4. Fault Bands

We have already described simple intergrowth defects, in which additional slabs of material are inserted parallel to one or other set of CS planes in the matrix. However, numerous observations of arrays of defects which extend through the crystals in other directions have now been made. The only restriction on the orientation of these defects appears to be that they all lie parallel to the short b axis, except for occasional steps, which were referred to briefly in Sect. 3.1.2. The arrays may consist of columns of single blocks, and an example is evident in Fig. 5a, where isolated 3×3 blocks occur along a line which is at an angle of about 33° to the a axis of the matrix. More frequently, they contain groups of blocks, which vary considerably in complexity. A simple example is found in Fig. 8a—the domain of $TiNb_{14}O_{37}$ marked A may be regarded as a fault band, consisting only of 5×3 blocks.

Some examples of more complex arrangements of blocks in fault bands are shown in Fig. 9. In Fig. 9a, the band contains 4×3 and 5×3 blocks which are misoriented with respect to the matrix —their long axes are perpendicular to those of blocks in the remainder of the fragment. Nevertheless, the blocks appear to fit together coherently, and the model in Fig. 9b confirms this. A considerable amount of symmetry exists within the fault band itself—for example, the point X is a center of symmetry for that region of the fault which is enclosed by a broken line in the corresponding model in Fig. 9b.

Figure 9c shows a fault band containing 4×4 and 5×3 blocks, which interrupts the matrix in yet another direction. Its structure contains a repeating unit of nine blocks, outlined in the model in Fig. 9d, except in the vicinity of R, where the band suffers a displacement, and a new type of block junction occurs. Another example of this type of junction is labeled R in Fig. 7a, and a row of them can be seen in the fault in Fig. 9e. This fault runs parallel to the c axis of the matrix, and it also contains a displacement with an associated change in fault structure, shown in the model in Fig. 9f.

A more detailed representation of the junction

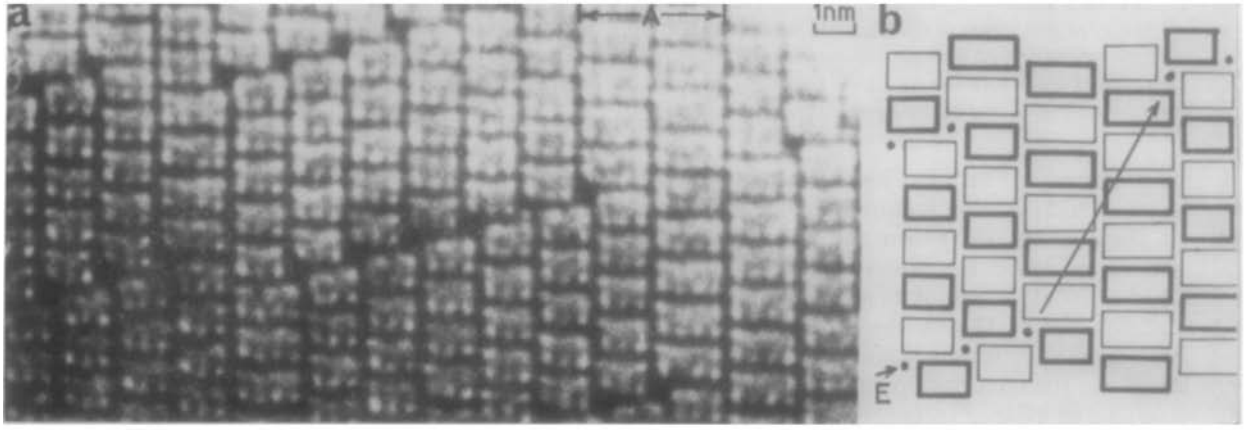

FIG. 8a. Lattice image, showing the intergrowth of narrow domains of 5×3 blocks of $TiNb_{14}O_{37}$, and the associated displacement of E planes containing tetrahedral sites (dark blobs). (b) Model of the region at the right end of (a). The arrow indicates the displacement of an E plane across the domain of 5×3 blocks.

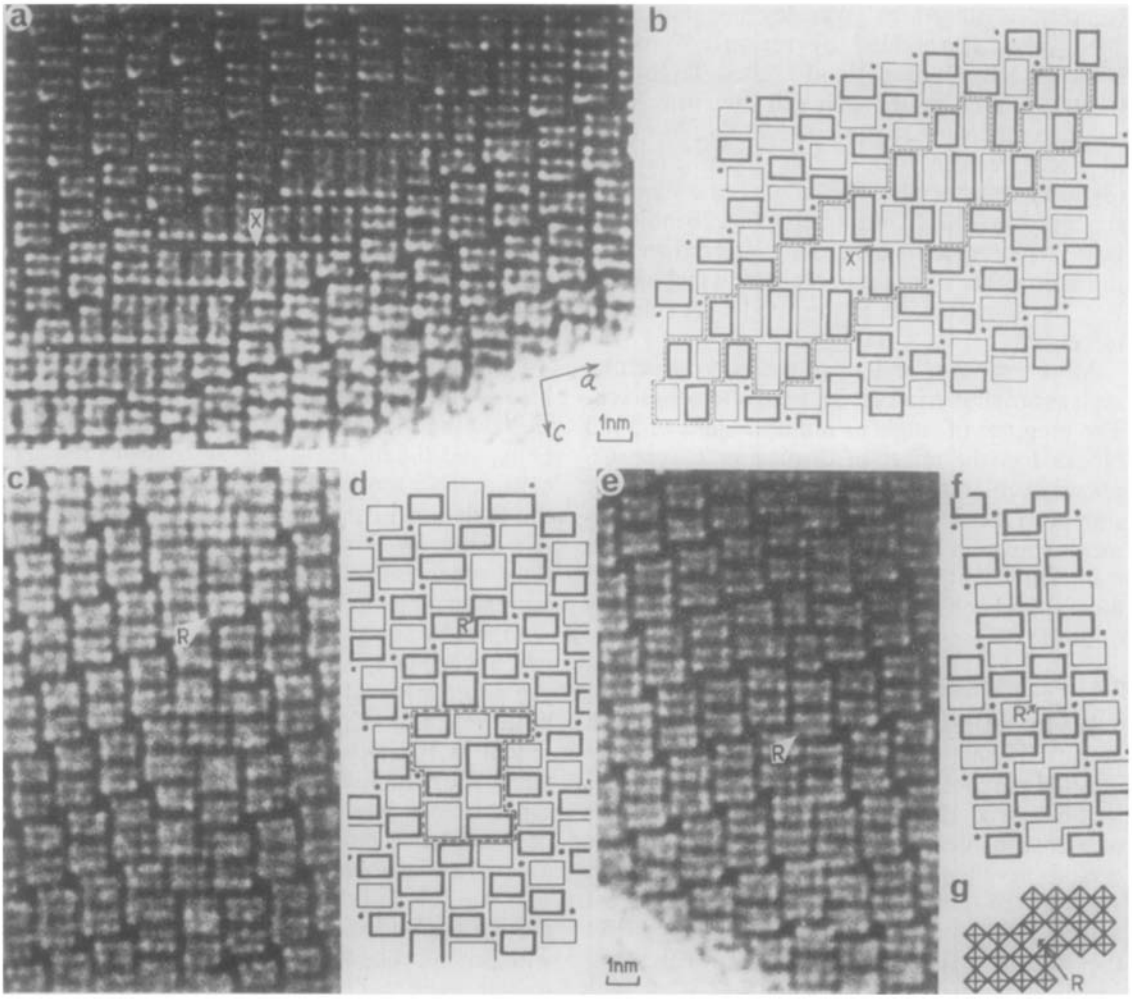

FIG. 9. Lattice images and idealized models of fault bands found in $TiO_2 \cdot 7Nb_2O_5$. In all cases, the matrix is $TiNb_{24}O_{62}$, and the magnification and matrix axes in (a) apply to all the micrographs. (a and b). The band contains 4×3 and 5×3 blocks whose long axes lie perpendicular to those of blocks in the matrix. The point *X* marks the center of symmetry of that region of the band which is outlined in (b). (c and d). The band contains 4×3, 4×4, and 5×3 blocks, and the repeating unit of fault structure is outlined in (d). This repetition is interrupted in the vicinity of *R*, which is a new type of block junction. (e–g). A row of *R*-type junctions occurs in this band, and the model in (g) shows detail of the proposed structure of these junctions.

R is shown in Fig. 9g. Close inspection of the images indicated that there were empty channels at these junctions, which the model suggests should be twice the size of those within the blocks. Block junctions of this kind have been found in $NaNb_{13}O_{33}$, in which the larger channels are occupied by sodium ions. Andersson *(20)* has discussed the relationship between this structure and that of $TiNb_{14}O_{37}$ in some detail.

It is evident from these examples that when the matrix is ordered and the fault band is linear, a repeating unit can be distinguished within it. The symmetry and periodicity of the band in these circumstances is an inevitable consequence of the preservation of orientation and symmetry in the matrix. Only when the band is displaced, or intersected by another fault, is its structure altered. A good example of these effects is shown in Fig. 10a. The band ABC is intersected by a domain of $Ti_2Nb_{10}O_{29}$ DB, and changes its direction as a consequence. The linear segments of the band, A and C, each have their own particular structure, shown in Fig. 10b. Within these segments, "unit cells" of the faulted

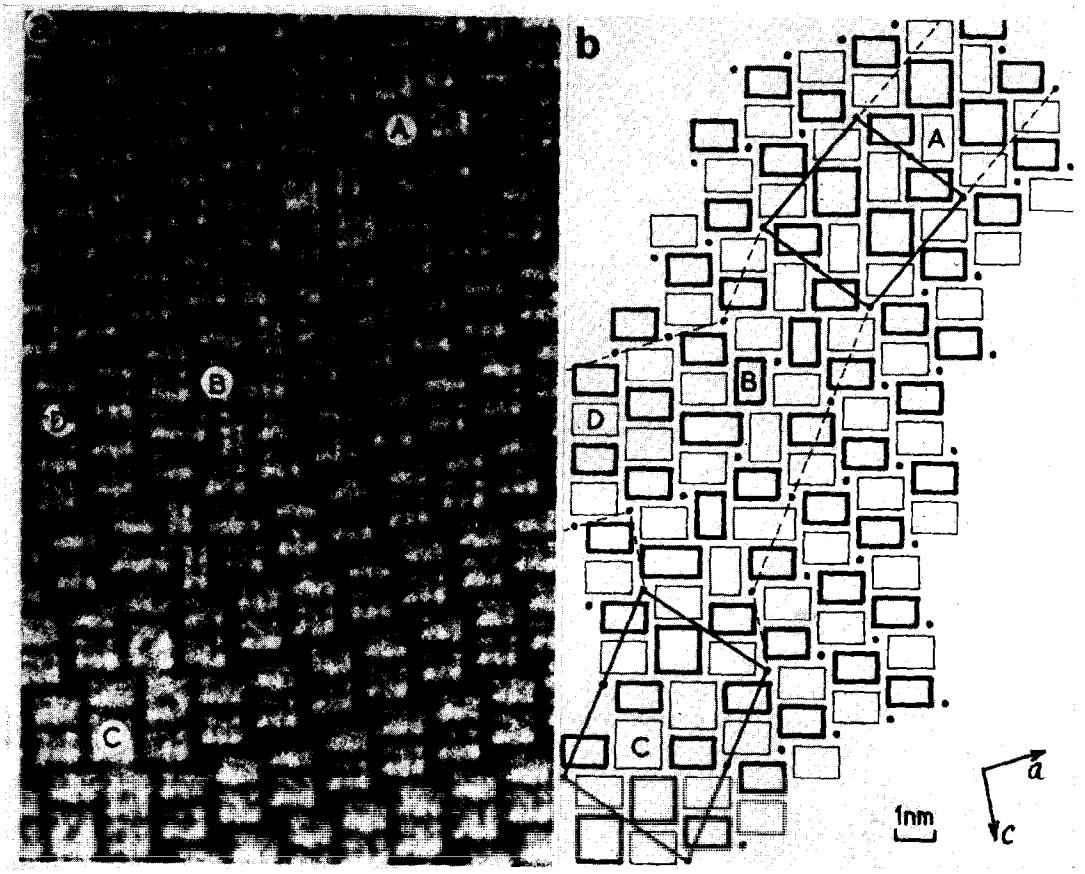

FIG. 10a. Lattice image, showing a microdomain of $Ti_2Nb_{10}O_{29}$ (D) terminating on a fault band ABC in a matrix of $TiNb_{24}O_{62}$. The structure of the fault band at A and C differs as a consequence of a change of direction in the neighborhood of B. (b). Model of the structure in (a), drawn to the same scale. The boundaries of the faulted region are marked by broken lines. "Unit cells" of the linear parts A and B of the fault band ABC are outlined. The axes refer to the matrix.

structure can be distinguished, and these are outlined in Fig. 10b. Their compositions, estimated by counting the atoms in these unit cells, are $3TiO_2 \cdot 25Nb_2O_5$ at A and $5TiO_2 \cdot 38Nb_2O_5$ at B. As might be expected, both regions, and also the Wadsley defect DB, are richer in TiO_2 than the matrix.

3.5. Grain Boundaries

Boundaries between crystals of different orientations were rare in the fractured fragments of material which we examined. Those which were observed always lay parallel to the *b* axis, and separated regions where the blocks were oriented perpendicular to each other. An example is shown in Fig. 11, and it is clear again that the boundary is coherent. It is obvious that coherent boundaries will only be possible for a small number of very specific orientation relationships between adjacent grains. It seems very likely that incoherent boundaries, if they exist in these materials, will be mechanically weak, and will act as preferred regions for fracture; we would therefore not expect to find them in ground fragments.

We noticed that the numbers of defects of all kinds tended to be highest in fragments which also contained a grain boundary, suggesting that perhaps nonstoichiometry in the crystals tends to concentrate in the boundary regions.

4. Discussion

4.1. Defect Structures

High resolution observations of the sample of $TiO_2 \cdot 7Nb_2O_5$ have enabled us to confirm the

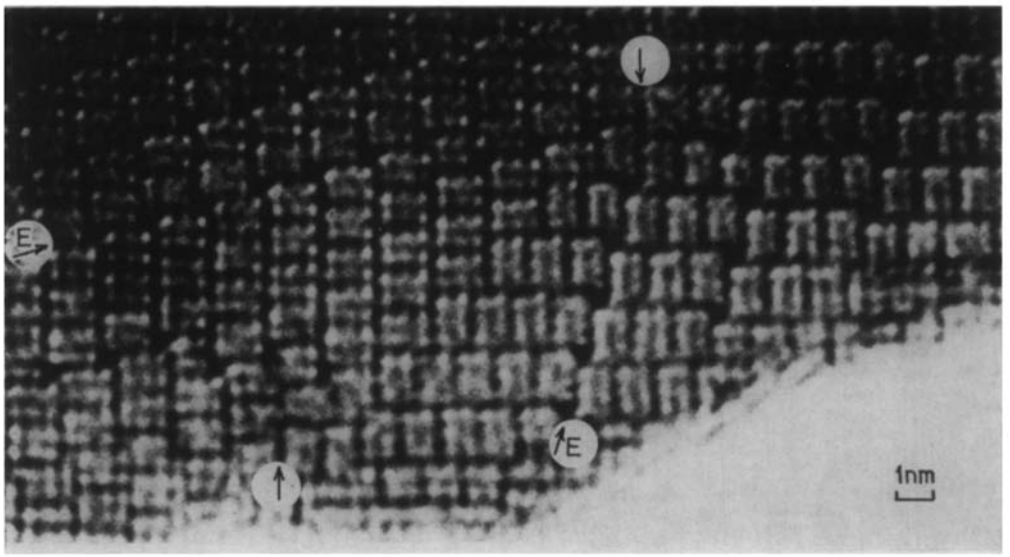

FIG. 11. Lattice image from a fragment of $TiO_2 \cdot 7Nb_2O_5$, showing a grain boundary (arrowed) separating regions where the long axes of 4 × 3 blocks lie perpendicular to each other. The identity and direction of an *E* plane, containing tetrahedral sites, is marked in each region.

proposed structures of Wadsley defects (*4*) and displacements (*9*), and to derive models for much more complex faults. The few examples we have given serve to illustrate the almost incredible versatility with which these block structures can accommodate a wide variety of arrangements in a coherent way. Most of these faulted regions are associated with a variation of stoichiometry from that of the matrix, and some of the observations tend to suggest that the faulted areas which occur within an ordered matrix, are metastable sinks, where the discrepancy in composition accumulates. For example, the micrographs in Figs. 9 and 10 show small sections of fragments in which the matrix was perfectly ordered $TiNb_{24}O_{62}$. The image from which Fig. 10a was taken showed a number of Wadsley defects similar to BD, all terminating on the fault band ABC, and beyond this bounding fault (i.e., to the right of Fig. 10a), the matrix was perfect. Given time at an appropriate temperature, one might expect the faulted region to become more and more confined, and at the same time richer in the excess component (TiO_2), leading finally to a separate grain of $Ti_2Nb_{10}O_{29}$. Similar arguments have been presented recently to explain the presence of domain structures in several polymorphs of Nb_2O_5, prepared by chemical transport (*21*). Networks of walls or fault bands surrounding ordered regions of matrix were attributed to the segregation of low levels of impurities.

On the other hand, micrographs such as those reproduced in Fig. 3 contain regions of ordered intergrowth with compositions intermediate between those of $TiNb_{24}O_{62}$ and $Ti_2Nb_{10}O_{29}$, and much closer to the nominal composition of the sample. There is therefore the possibility that under suitable conditions, the sample might finally achieve a homogeneous structure, in which the intergrowth of component slabs of the two terminal compositions appropriately matches the overall stoichiometry. It is very obvious that the sample which we have studied is not a suitable one from the point of view of obtaining an answer to the question "what is the equilibrium situation?" There is a continuing need for precise studies of the kind which will resolve this question, but our experiments indicate that these studies will probably be tedious and time consuming. It seems clear that the free energy differences between a perfectly ordered arrangement and the disordered and faulted structures which we have described, will be quite small, and that the attainment of true equilibrium will be very slow indeed.

4.2. High Resolution Electron Microscopy

The potential of the lattice imaging technique as a means for studying periodic and defect structures directly has been recognized for many years, but recent attempts to apply it to the observation of dislocations in metals (*22*, *23*) have been the subject of criticism on theoretical

grounds (*24*). There is no doubt, however, that in the case of the complex niobium oxides, we have obtained images which truly reflect structure, first at the unit cell level (*2*, *4*, *9*), and now at almost the atomic level. We believe that there are two important factors which have contributed to the successful application of the method to these materials:

a. We have chosen orientations in which the significant structural features, such as CS planes and blocks of octahedra containing empty channels, lie parallel to the incident electron beam, and do not overlap seriously in projection. This "minimum overlap" criterion is particularly easily satisfied in the present case, because of the short (0.38 nm) *b* axis, and the simplicity of the structure in this direction.

b. The complex oxides have large unit cells, and therefore many diffracted beams contribute to the image, even when the objective aperture diameter is restricted in order to reduce the effect of spherical aberration.

These factors are discussed in more detail elsewhere (*25*).

Acknowledgments

One of the authors (S. I.) thanks Professor J. M. Cowley for his continuous encouragement, and acknowledges the support of a USNSF Area Development Grant in Solid State Science (No. GU 3169). We are grateful to Mr. M. O'Keefe of CSIRO, for permission to reproduce a computed lattice image, which is inset in Fig. 2.

References

1. A. D. WADSLEY AND S. ANDERSSON, *in* "Perspectives in Structural Chemistry" (J. D. Dunitz and J. A. Ibers, Eds.), Vol. III. Wiley, New York (1970).
2. J. G. ALLPRESS, J. V. SANDERS, AND A. D. WADSLEY, *Acta Crystallogr., Sect. B* **25**, 1156 (1969).
3. J. G. ALLPRESS AND A. D. WADSLEY, *J. Solid State Chem.* **1**, 28 (1969).
4. J. G. ALLPRESS, *J. Solid State Chem.* **1**, 66 (1969).
5. J. G. ALLPRESS AND J. V. SANDERS, *in* "Electron Microscopy and Structure of Materials" (G. Thomas, Ed.). Univ. of California Press, Berkeley (1972).
6. S. IIJIMA, *J. Appl. Phys.* **42**, 5891 (1971).
7. J. M. COWLEY AND S. IIJIMA, *Z. Naturforsch.* **27a**, 445 (1972).
8. A. D. WADSLEY, *Acta Crystallogr.* **14**, 664 (1961).
9. J. G. ALLPRESS, *J. Solid State Chem.* **2**, 78 (1970).
10. J. G. ALLPRESS AND R. S. ROTH, *J. Solid State Chem.* **3**, 209 (1971).
11. R. S. ROTH AND A. D. WADSLEY, *Acta Crystallogr.* **18**, 724 (1965).
12. J. G. ALLPRESS, *Mater. Res. Bull.* **4**, 707 (1969).
13. M. A. O'KEEFE, unpublished data.
14. J. G. ALLPRESS, E. A. HEWAT, A. F. MOODIE, AND J. V. SANDERS, *Acta Crystallogr., Sect. A*, **28**, 528 (1972).
15. D. F. LYNCH AND M. A. O'KEEFE, *Acta Crystallogr., Sect. A*, **28**, 536 (1972).
16. B. M. GATEHOUSE AND A. D. WADSLEY, *Acta Crystallogr.* **18**, 724 (1965).
17. S. ANDERSSON, *Z. Anorg. Allg. Chem.* **351**, 106 (1967).
18. A. D. WADSLEY, *Acta Crystallogr.* **14**, 660 (1961).
19. M. LUNDBERG, *J. Solid State Chem.* **1**, 463 (1970).
20. S. ANDERSSON, *Acta Chem. Scand.* **19**, 557 (1965).
21. J. S. ANDERSSON, J. M. BROWNE, AND J. L. HUTCHISON, *Nature (London)* **237**, 151 (1972).
22. J. R. PARSONS AND C. W. HOELKE, *J. Appl. Phys.* **40**, 866 (1969).
23. V. A. PHILLIPS AND J. A. HUGO, *Acta Met.* **18**, 123 (1970).
24. D. J. H. COCKAYNE, J. R. PARSONS, AND C. W. HOELKE, *Phil. Mag.* **24**, 139 (1971).
25. J. G. ALLPRESS AND J. V. SANDERS, *J. Appl. Crystallogr.*, in press (1973).